Supplementary Material

Text S1. Coseismic Static Stress Change

The Coulomb Failure Stress (ΔCFS) change on the nearby faults can be expressed as:

$$\Delta CFS = \Delta\tau_s + \mu'\Delta\sigma_n \qquad \text{(Eq2)}$$

Where $\Delta\tau_s$ and $\Delta\sigma_n$ are the shear and normal stress changes, respectively. μ′ is the effective friction coefficient, usually use between 0.2 and 0.8 [1]. Since the 2021 Maduo earthquake is almost a pure strike-slip event, the initial setting in this study is 0.4 [2].

According to the elastic dislocation theory, the static stress changes caused by seismic slip can be calculated [3]. The corresponding changes in normal stress and shear stress can be calculated by projecting it onto a specific direction (receiver fault). In this study, the layered Earth model was the same as that used in the joint inversion. We performed PSGRN/PSCMP [4] software to calculate the coseismic ΔCFS change with depth (Figure S4).

The coseismic ΔCFS change with depth caused by the Maduo earthquake, as a whole, was characteristic of the typical strike-slip stress distribution with a 4-parttern loading and unloading zones. The cumulative stress on the northern and southern walls of the fault was obviously released, and both are greater than 1 bar, while the stress on the eastern and western endings was significantly loaded. In addition, the stress loading zone along the fault was highly correlated spatially with the post-seismic after-slip region [5,6]. We speculate that the cumulative stress on the fault was not fully released in the main shock, and then promoted the aftershocks and post-seismic after-slip [7,8].

Supplementary Figures

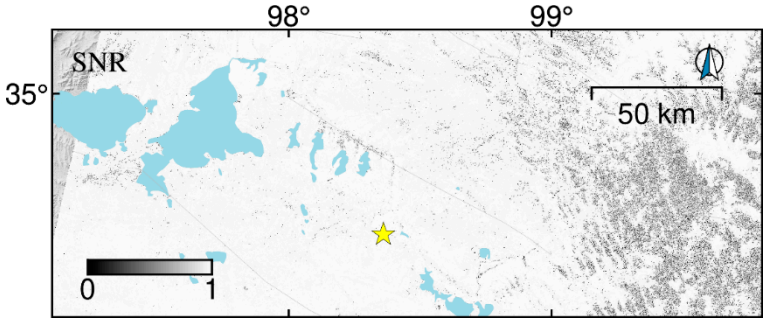

Figure S1. Signal to Noise Ratio distribution of optical deformation fields in the Sub-Pixel Correlation process.

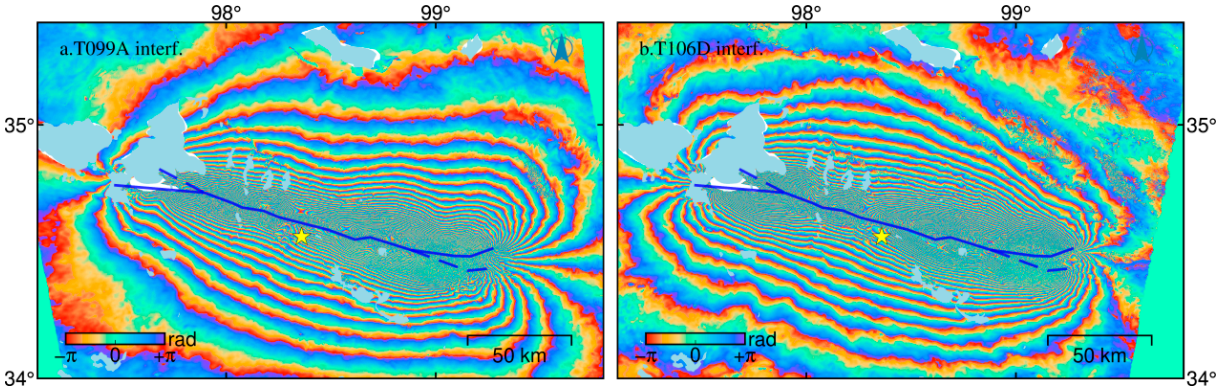

Figure S2. Ascending and descending coseismic interferogram of Maduo earthquake.

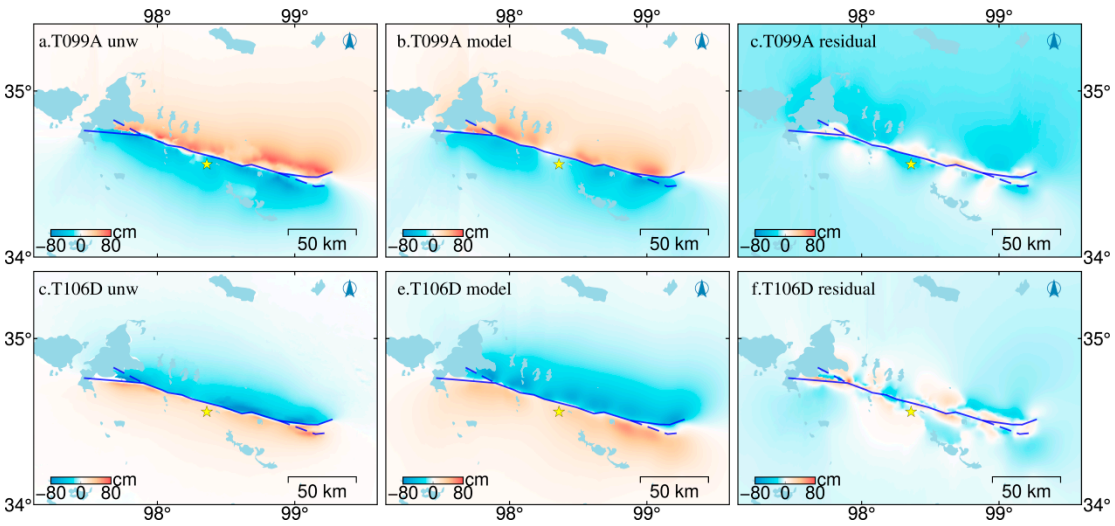

Figure S3. Fitting of fault slip model and observed values.

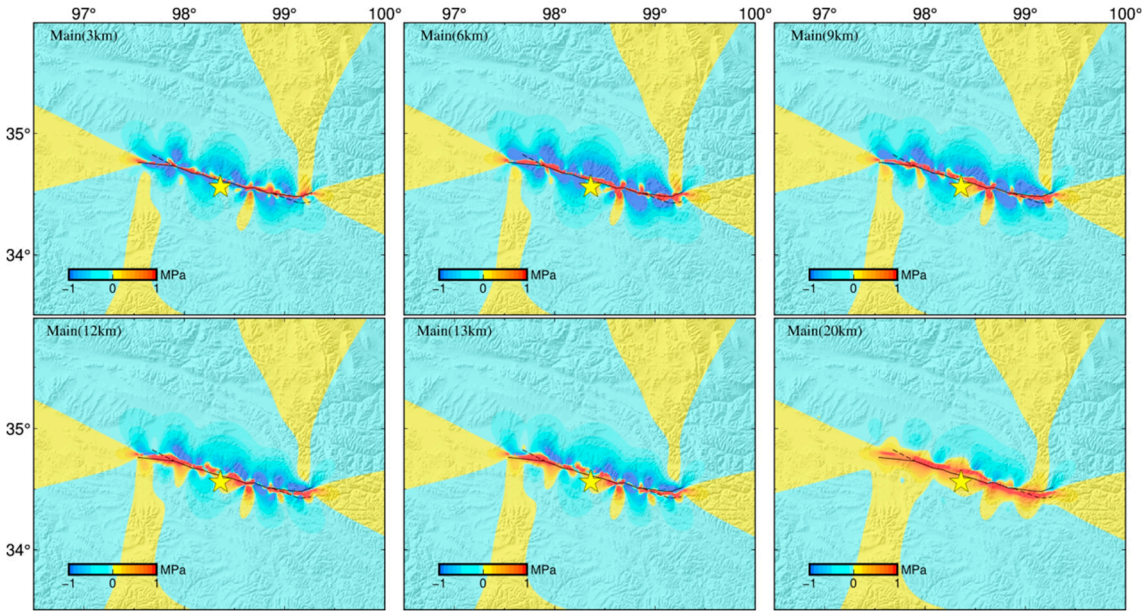

Figure S4. Coseismic Coulomb stress changes at different depths for the 2021 Maduo earthquake (a-d) and Static Coulomb stress changes induced by the main shock using the tail branches as the received faults (e). Yellow star indicates the epicenter. Black solid and dashed lines indicate the main and branch faults. Black circles mark aftershocks eight days after the main shock [9].

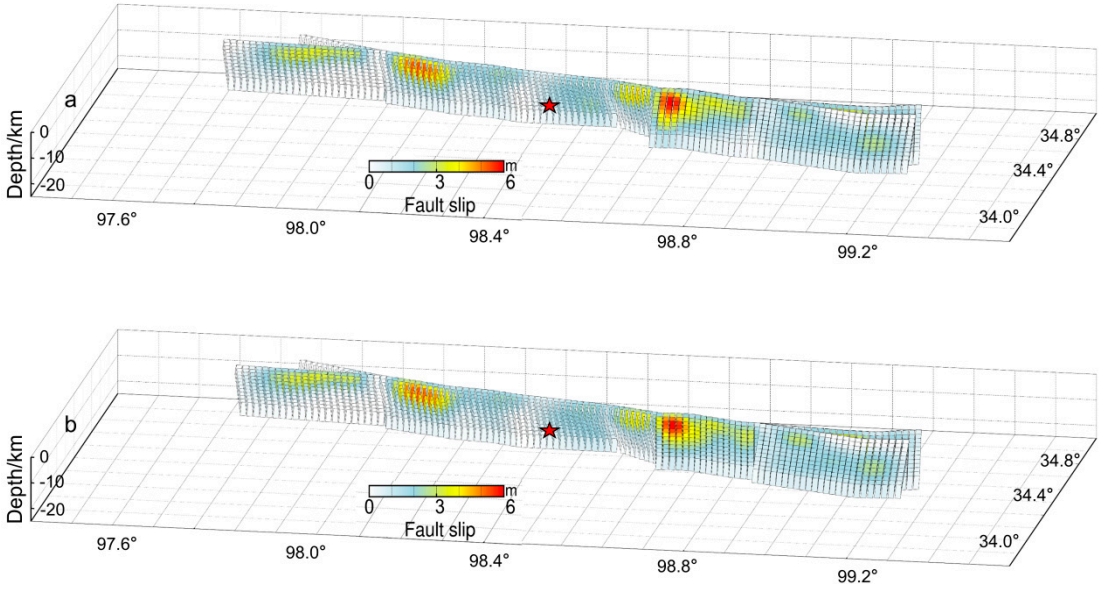

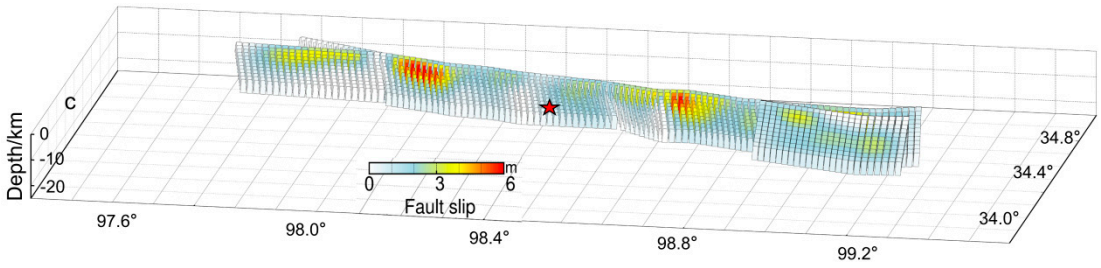

Figure S5. Fault slip distribution model of different S.6 dip; a-80°S、b-90°、c-80°N .

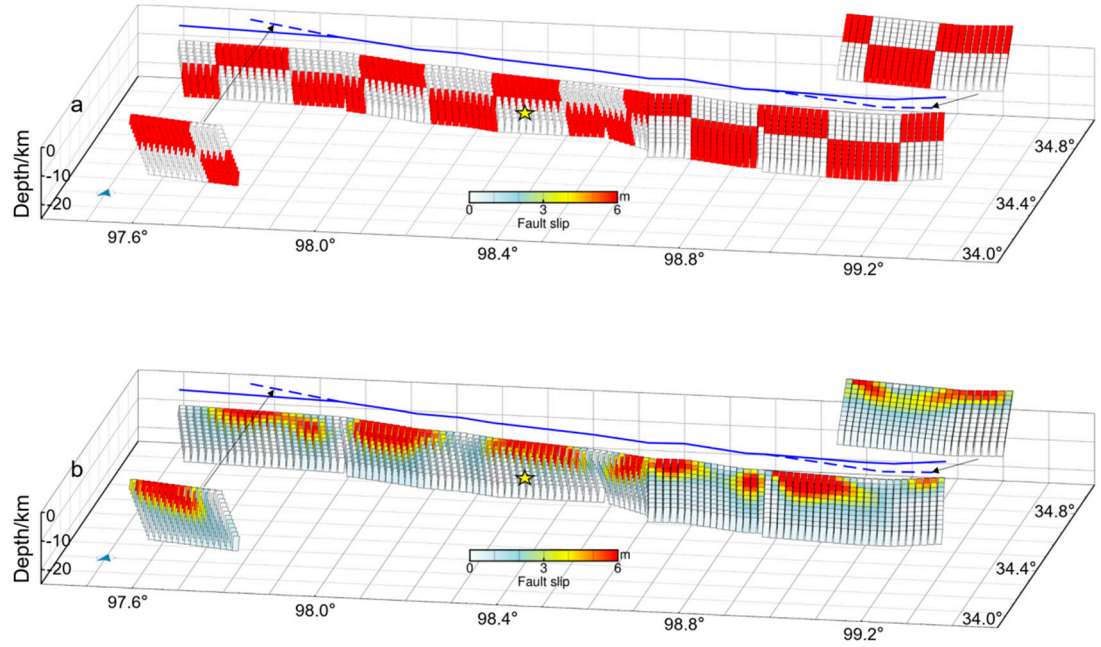

Figure S6. Checkerboard tests of the slip distribution. (a) The synthetic slip model used in the sensitivity test and the slip inferred by inverting for the synthetic dataset corresponding to the slip model under the assumption that the fault geometry and the optimal smoothing parameters are fixed. (b) Inversion of slip distribution based on deformation caused by (a) slip distribution.

To illustrate the extent to which the SAR images can constrain the resolution of the slip model and show uncertainties of the slip and trade-offs of slips between different patches, we conducted a checkerboard test. The size of each checkerboard grid was approximately 10.5 km × 10 km, and the input model assumed pure strike slip of 6 m along arbitrarily chosen slip patches to ensure a cumulative moment consistent with that of the actual slip model (Figure S6-a). We first computed the synthetic displacements for data points in the resampled LOS maps from the synthetic slip model and added some noise. Then, using the same fault geometry and regularization penalty parameters as those employed in the actual inversion, the coseismic slip distribution was inverted from the synthetic dataset (Figure S6-a). For the synthetic slip model, the shallow asperities

can be distinguished in magnitude (Figure S6-b), although some areas with large strike trend changed were poorly identified . In contrast, the deep asperities rarely recovered, and a high degree of smoothing is observed between the deep slip patches. Our resolution test thus demonstrates a reasonable resolution to retrieve the shallow, strike trend smooth asperities from low-slip zones, implying that the pattern of slip can be resolved under these conditions.

Supplementary Tables

Table S1. Geodetic data used in this study.

Sensor	Track	Incidence	Azimuth	Pass	Tile Identifier	Master	Slave	Days after Mainshock	Processing method
Sentinel-1	099	39°	347°	Asc	—	8 May 2021	26 May 2021	4	D-InSAR
	106	39°	193°	Des	—	20 May 2021	26 May 2021		
	106	39°	193°	Des	—	20 May 2021	1 Jun. 2021	10-34	Phase Gradient
					—	20 May 2021	13 Jun. 2021		
					—	20 May 2021	25 Jun. 2021		
Sentinel-2	47	—	—	—	T47SLU	12 Oct. 2020	17 Oct. 2021	148	SPC (Sub-pixel correlation)
		—	—	—	T47SMU				
		—	—	—	T47SNU				
UAV imagery								3~20	Manual interpretation

Table S2. The fault slip distribution model caused by different dip of S.6.

S.6 dip	Maximum slip at east and west sections		Model fit/%
	S.3	S.6	
80°S	5.24	5.08	93.17
90°	5.25	5.99	93.09
80°N	5.31	5.98	92.87

To search the best dip of S.6, we carried out many inversions on dip of S.6 by trial-and-error tests. Some results are shown in Table S2. Although the fit degree between models and observation is improved as dip of the S.6 varies from north to sourth. However, locations of the maximum coseismic slip change accordingly from east to west, which indicates dip

which contradict the most results of previous scholars. Therefore, we finally select the second project, 90°, as the S.6 dip.

Table S3. The fault slip distribution model caused by different dip of bifurcation on the east and west sides.

Dip of bifurcation on the east and west sides				Maximum slip at east and west sides of the epicenter		Model fit/%
S.1	S.2	S.7	S.8	west	east	
N	N	S	S	6.00(S.3)	6.00(S.6)	88.29
N	N	N	S	6.00(S.3)	6.00(S.6)	87.97
N	N	S	N	5.13(S.3)	6.00(S.5)	87.45
S	N	S	S	3.95(S.3)	5.88(S.5)	87.13
N	S	S	S	6.00(S.3)	6.00(S.5)	88.06

To get the best project of the dip of bifurcation on the east and west sides, we change the S.1、S.2、S.7、S.8 dip toward to inverse the fault slip model. Notice: the dataset we inversed in Table S3 was not good as we finally used in article. As shown in Table S2, some project maximum slip is 6.00, which reached the upper bound of maximum slip we set before inversion. However, our experiments still made sense. Compared the five projects, we can find the first project have the highest model fit. Other projects changed one dip toward of the four bifurcation segments, but the model fit were all lower than the first. In the end, we select the first project with the better dataset, used in Table S.1, to inverse fault slip and get the proper result.

Table S4. The layer Earth models employed in inversion

	Depth(km)	V_p(km/s)	V_s(km/s)	Density(kg/m^3)
1	0~4	5.2	2.9	2400
2	4~19.7	5.8	3.4	2600
3	19.7~27.2	6.0	3.5	2700
4	27.2~35.2	6.1	3.6	2700
5	35.2~44.7	6.3	3.7	2800

6	44.7~58.2	6.5	3.8	3000
7	58.2~	8.0	4.6	3400

References:

1. Parsons, T.; Stein, R.S.; Simpson, R.W.; Reasenberg, P.A. Stress sensitivity of fault seismicity: A comparison between limited-offset oblique and major strike-slip faults. *Journal of Geophysical Research Solid Earth* **1999**, *104*, 20183-20202.
2. Xiong, X.; Shan, B.; Yong, Z.; Wang, R. Stress transfer and its implication for earthquake hazard on the Kunlun Fault, Tibet. *Tectonophysics* **2010**, *482*, 216-225.
3. Yoshimitsu, O. Internal deformation due to shear and tensile faults in a half-space. *Bulletin of the Seismological Society of America* **1992**.
4. Wang, R.; Lorenzo-Martín, F.; Roth, F. PSGRN/PSCMP—a new code for calculating co- and post-seismic deformation, geoid and gravity changes based on the viscoelastic-gravitational dislocation theory. *Computers & Geosciences* **2006**, *32*, 527-541.
5. Fang, J.; Ou, Q.; Wright, T.J.; Okuwaki, R.; Amey, R.M.J.; Craig, T.J.; Elliott, J.R.; Hooper, A.; Lazecký, M.; Maghsoudi, Y. Earthquake Cycle Deformation Associated With the 2021 MW 7.4 Maduo (Eastern Tibet) Earthquake: An Intrablock Rupture Event on a Slow-Slipping Fault From Sentinel-1 InSAR and Teleseismic Data. *Journal of Geophysical Research: Solid Earth* **2022**, *127*, e2022JB024268, doi:https://doi.org/10.1029/2022JB024268.
6. ZHAO, L.; XU, W.; FANG, N.; LIU, J.; FENG, G. Coseismic and early postseismic fault slip model and the seismogenic fault friction properties of the 2021 Qinghai Madoi Mw7.3 earthquake(in Chinese). *Chinese Journal of Geophysics* **2023**, *66*, 1086-1097.
7. He, L.; Feng, G.; Wu, X.; Lu, H.; Xu, W.; Wang, Y.; Liu, J.; Hu, J.; Li, Z. Coseismic and Early Postseismic Slip Models of the 2021 Mw 7.4 Maduo Earthquake (Western China) Estimated by Space‐Based Geodetic Data. *Geophysical Research Letters* **2021**, *48*, e2021GL095860, doi:10.1029/2021gl095860.
8. Xiong, W.; Chen, W.; Wang, D.; Wen, Y.; Nie, Z.; Liu, G.; Dijin, W.; Yu, P.; Qiao, X.; Zhao, B. Coseismic slip and early afterslip of the 2021 Mw 7.4 Maduo, China earthquake constrained by GPS and InSAR data.

Tectonophysics **2022**, *840*, 229558,
doi:https://doi.org/10.1016/j.tecto.2022.229558.